Capturing "Extraordinary" Soft-Assembled Charge-Like Polypeptides as a Strategy for Nanocarrier Design

Aroa Duro-Castano, Vicent J. Nebot, Amaya Niño-Pariente, Ana Armiñán, Juan J. Arroyo-Crespo, Alison Paul, Natalia Feiner-Gracia, Lorenzo Albertazzi, and María J. Vicent**

The rational design of nanomedicines is a challenging task given the complex architectures required for the construction of nanosized carriers with embedded therapeutic properties and the complex interface of these materials with the biological environment. Herein, an unexpected charge-like attraction mechanism of self-assembly for star-shaped polyglutamates in nonsalty aqueous solutions is identified, which matches the ubiquitous "ordinary–extraordinary" phenomenon previously described by physicists. For the first time, a bottom-up methodology for the stabilization of these nanosized soft-assembled star-shaped polyglutamates is also described, enabling the translation of theoretical research into nanomaterials with applicability within the drug-delivery field. Covalent capture of these labile assemblies provides access to unprecedented architectures to be used as nanocarriers. The enhanced in vitro and in vivo properties of these novel nanoconstructs as drug-delivery systems highlight the potential of this approach for tumor-localized as well as lymphotropic delivery.

Nanomedicine and nanotechnology have emerged to address unmet medical needs in cancer treatment[1] and recently expanded into other areas including neurological disorders or infectious diseases.[2] The translation of nanoproducts to routine clinical use has demonstrated their potential.[3] A nanocarrier size range between 20 and 100 nm is optimal to enhance blood circulation times and promotes an effective passive targeting by the "enhanced permeability and retention (EPR) effect."[4] This
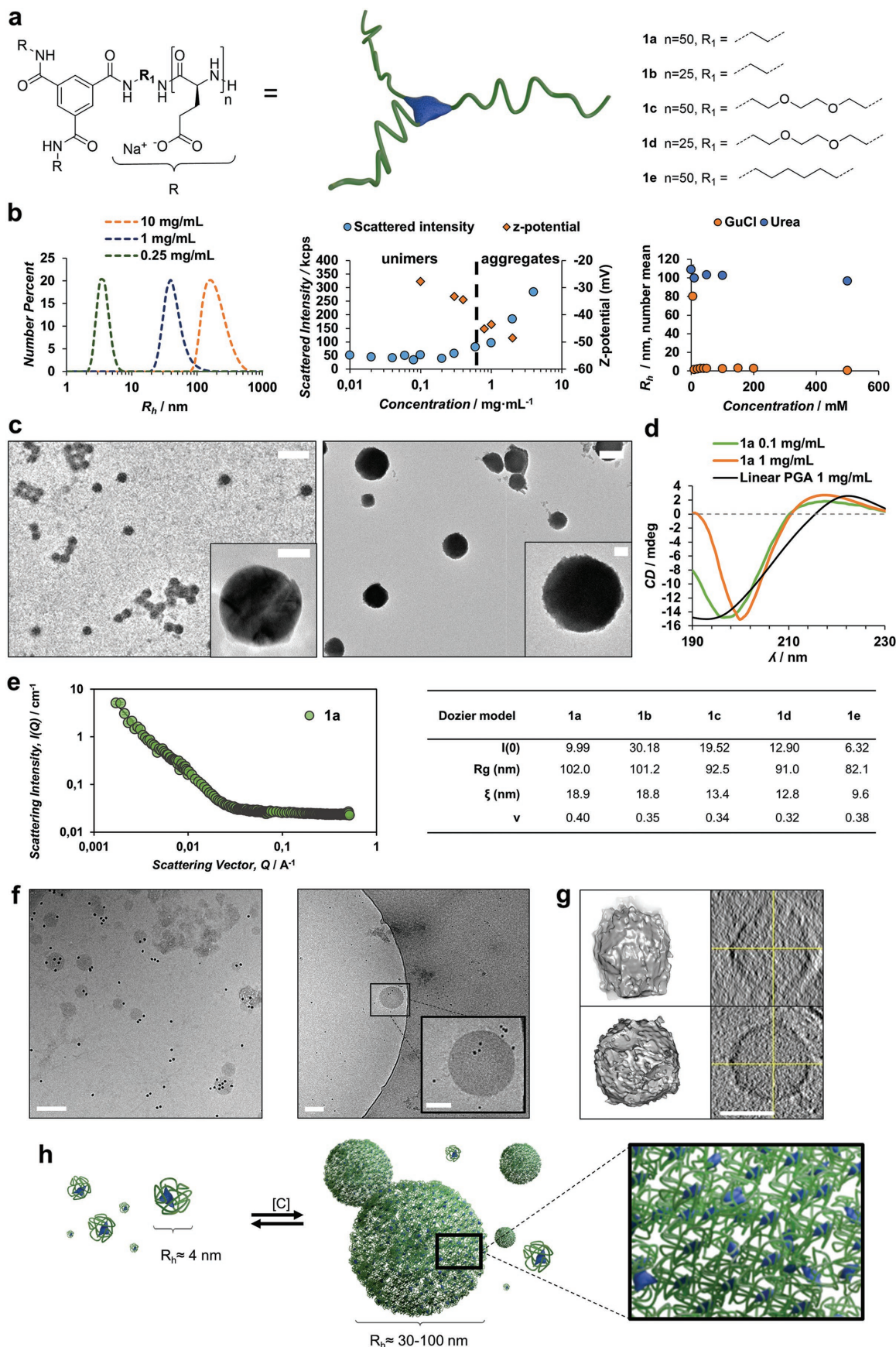
Dr. A. Duro-Castano, Dr. V. J. Nebot, A. Niño-Pariente,
Dr. A. Armiñán, J. J. Arroyo-Crespo, Dr. M. J. Vicent
Polymer Therapeutics Laboratory
Centro de Investigación Príncipe Felipe
Av Eduardo Primo Yúfera 3, 46012 Valencia, Spain
E-mail: vnebot@cipf.es; mjvicent@cipf.es
Dr. A. Paul
School of Chemistry
Cardiff University
Main Building, Park Place, Cardiff CF10 3AT, UK
N. Feiner-Gracia, Dr. L. Albertazzi
Institute for Bioengineering of Catalonia (IBEC)
The Barcelona Institute of Science and Technology
Carrer de Baldiri Reixac 15-21, 08028 Barcelona, Spain

size range can be achieved by the use of higher molecular weight (MW) biodegradable carriers or the self-assembly of individual unimeric species to yield larger nanostructures. Acquired knowledge in the design of drug delivery systems (DDSs) is raising awareness about the need for fully biodegradable and biocompatible carriers.[5] In this framework, well-defined polypeptides with advanced engineered complexity and structural versatility arise as perfect candidates with proven therapeutic potential and clinical translation.[6] The intrinsic architectural, conformational, and multifunctional properties of branched polypeptides, inaccessible to linear polymers, together with their tunable and feature accelerated manufacture compared to dendrimers, make their application as DDS a potentially exciting proposition.[7]

The rising potential of polymer self-assembled DDS is nowadays only limited to mastering the molecular interactions such as hydrophobic effect, host–guest or electrostatic interactions, among others.[8] While seemingly counterintuitive, charge-like macromolecule aggregation has been described from a theoretical standpoint[9] and represents a ubiquitous phenomenon in biology, involved, for example, in virus capsid and microtubule (F-actin) self-assembly, DNA condensation, and chromosome motion.[10] The successful integration of mean field, counterion condensation, and Flory theories for polyelectrolyte solution has shed light on this self-assembly phenomenon.[11–13] Experimental evidence for charge-like attraction arises from the observation of two diffusional regimes, the "fast" and "slow" modes observed from dynamic light-scattering (DLS) experiments.[13,14] Particularly relevant for the present work is the "slow" mode, also referred as "extraordinary" behavior, where polyions experience attraction at certain concentrations and low salt content to yield aggregated species. Experimental reports of such aggregation mechanism have mainly been reported from scattering techniques and approached from a theoretical standpoint. This may be due to the transient, disordered, and reversible nature of these soft materials, which not only makes sample manipulation and observation difficult, but also hinders their applicability.

In our attempts to develop improved nanosized DDSs based on star-shaped polyglutamates, we identified this unexpected charge-like attraction mechanism of self-assembly. In this study, we used a wide array of techniques to provide consistent

1702888 (2 of 12)

experimental evidence for the "extraordinary" behavior. For the first time, we show how a bottom-up methodology reliant on the molecular design and covalent stabilization of highly dynamic coassemblies via "extraordinary" behavior allows the construction of otherwise inaccessible nanostructures of 30–100 nm in radius, a size ideal to promote long-blood circulation times and enhanced therapeutic effect, particularly in cancer treatments.

We synthesized a family of well-defined 1,3,5-benzenetricarboxamide (BTA)-centered star-shaped polyglutamates (sodium salts) with control on target degree of polymerization, narrow MW distributions, and arm length symmetry in a reproducible and scalable manner (**Figure 1**a and synthetic details in the Supporting Information).[15] Synthesized compounds differed structurally on the polyglutamate degree of polymerization with ≈25 or 50 glutamic units per arm and a BTA core motif bearing different spacers (Figure 1a, compounds **1a–e**). To gain a deep understanding of these systems and to acknowledge industrial and clinical translation concerns, we performed a detailed characterization of the compound **1** family. DLS measurements in deionized aqueous solutions for compound **1a** revealed nanosized objects with a concentration dependent hydrodynamic radius (R_h) in the range of 4–200 nm (Figure 1b, left). The smaller size must be attributed to star-polyglutamate unimers[15,16] whereas the increase in R_h to 40 and 200 nm observed at 1 and 10 mg mL^{-1}, respectively, suggested an unexpected self-association of unimers. We also observed a large critical aggregation concentration (CAC) compared to amphiphilic block copolymers, as derived from the scattered intensity versus concentration measurements (CAC ≈ 0.5 mg mL^{-1}, Figure 1b, middle).[17] Below the CAC, compound **1a** was present as an anionic unimeric specie with a negative z-potential from −25 to −35 mV. Above the CAC, we recorded a sharp increase in the scattered light and the negative z-potential. Of note, the linear counterpart displayed no evidence of this self-assembly behavior at the concentrations studied (Figure S23, Supporting Information). Tested derivatives from compound **1a** presented CAC values in the same range, independently of the core nature or arm length (Figure S23, Supporting Information). Transmission electron microscopy (TEM) images (also see Figure S24 in the Supporting Information) confirmed the existence of nanosized spherical aggregates of 50–100 and 200–300 nm in size for **1a** at 1 mg mL^{-1} (Figure 1c, left)

and 10 mg mL^{-1} (Figure 1c, right), respectively, in agreement with DLS data. A closer inspection of morphology evidenced low material density and amorphous nature, as confirmed by the flat X-ray powder diffraction pattern registered for freeze-dried samples of **1a** in H$_2$O (Figure S26, Supporting Information).

Although BTA is a widely used self-assembling motif that can induce defined molecular ordering within different supramolecular materials,[18] it requires hydrophobic groups to promote self-assembly in aqueous media.[19] At the molecular level, all attempts to prove the role of BTA in the self-assembly process, performed by fluorescence spectroscopy employing hydrophobic probes (pyrene and Nile Red, Figure S27 and S28, Supporting Information) or small-angle neutron scattering (SANS) contrast experiments of compound **3** (Figure S32, Supporting Information), failed to provide evidence of enriched BTA stack domains.[20] Our findings suggested a poor molecular order in the assemblies and the null participation of the BTA motif in driving the self-association process, as one would expect, since it only represents a small molar fraction of our system. However, circular dichroism (CD) allowed the identification of a characteristic feature for compound **1a**, with a recurrent redshift of the negative band at 200 nm above the CAC (Figure 1d and Figure S34, Supporting Information). This small shift was most likely generated due to partial constraint or orientation of the arms within the assemblies rather than small coil to helix transition of polyglutamate secondary structure upon partial protonation of carboxylic acids, which was negligible at the working pH (Figure S42 and Table S10, Supporting Information). We note that size values did not experience significant changes in a physiologically relevant pH range (from pH 5 to 8) (see Figure S35 in the Supporting Information). In order to disprove the existence of intra- or intermolecular H-bonding along the polypeptidic backbone, we performed DLS titration experiments using common denaturants. Figure 1b (right) demonstrated that while assembly size did not significantly change following the addition of the nonionic denaturant urea, we observed rapid salt-mediated disassembly upon addition of ionic guanidinium chloride at low concentrations (10 × 10^{-3} M) or salts of opposite nature within the Hofmeister series (Figure S36, Supporting Information).[21] This experiment was key in elucidating the driving forces ruling the polyion

Figure 1. Self-assembly of star-shaped poly(L-glutamates) in aqueous media. a) BTA centered star-shaped poly(L-glutamates) (compounds **1a–c**) have been synthesized through ring opening polymerization of *N*-carboxyanhydride methodology (see the Supporting Information for synthetic and characterization details). b) Dynamic light scattering analysis of compound **1a** in ddH$_2$O demonstrates the dependence of the aggregation behavior on concentration (left panel) with a critical aggregation concentration estimated at around 0.5 mg mL^{-1} and a sharp decrease in z-potential value recorded (center panel, also see Figure S23 in the Supporting Information). Variable ionic strength experiments employing denaturating guanidinium chloride (GuCl) demonstrates assembly disruption to unimers at low salt concentrations (10 × 10^{-3} M) for compound **1a** (2 mg mL^{-1}) not observed when a nonionic denaturating analog such as urea was employed (right panel, also see Figure S35 and S36 in the Supporting Information). c) TEM images show the presence of 50–100 nm spherical particles in water at 1 mg mL^{-1} (left panel scale bar 200 nm, inset scale bar 50 nm) and up to 200–300 nm size at increased concentration of 10 mg mL^{-1} (right panel scale bar 200 nm, inset scale bar 50 nm), in good agreement with concentration dependence size observed by DLS (see Figure S24 in the Supporting Information for more TEM images). d) Circular dichroism shows a small redshift in the negative band of the random coil conformation of **1a** and above the CAC value (also see Figure S34 in the Supporting Information). e) Small angle neutron scattering (SANS) data analysis for compound **1a** (see full data in Figure S29 in the Supporting Information). Table displays the best-fit for the Gaussian coil for a Dozier star polymer model for compounds **1a–1e**. f) Cryo-TEM images of compound **1a** in aqueous solution (2 mg mL^{-1}) suggests a spherical assembly geometry with sizes ranging from ≈50 to 150 nm in diameter (scale bars: left and right panels are 100 nm, right inset is 50 nm, dense black spheres are 6 nm nanogold particles). g) 3D reconstructed tomograms from the same sample (scale bar: 50 nm, additional 3D reconstructions displayed in Figure S25 in the Supporting Information). h) The proposed aggregation equilibrium model based on all the data registered within the present study.

**ADVANCED
SCIENCE NEWS**

www.advancedsciencenews.com

**ADVANCED
MATERIALS**

www.advmat.de

self-assembly observed in our system and suggested ionic interactions as the main actors.

Cryo-TEM imaging for compound **1a** confirmed the existence of spherical objects of 30–100 nm in radius (Figure 1f). Visualization of isolated objects permitted the acquisition of tomographic series and 3D reconstruction of the selected nanoparticle (Figure 1g). We noted that the low contrast appearance and the homogeneous low electron density along the aggregate's structure discounted the existence of a defined core–shell. Furthermore, the irregular surface and globular geometry deviated from ideal spheres (additional 3D tomogram in Figure S25 in the Supporting Information), probably due to the dynamic and loose nature of the assemblies. Analysis of data acquired from SANS experiments for compounds **1a–e** in D_2O (Figure 1e) demonstrated a best fit for the "Gaussian coil for a Dozier star polymer" model.[22] Fitted parameters revealed a radius of gyration (R_g) of 80–100 nm matching the data obtained for compound **1a** via DLS and electron microscopy and again suggested the self-association of unimeric species. In the absence of interparticle interactions (where the interparticle structure factor value is $S(Q) = 1$, see Figure S29 in the Supporting Information for more details), the Flory component value variation (ν) was found to be small (close to $\frac{1}{3}$), indicating a relatively poor solvent and suggested that the studied polymers were in a collapsed conformation (dense stars). Furthermore, packing close to the core was influenced by the packing efficiency of the substituents (i.e., the polymer packed around a larger overall excluded volume for ethyl than hexyl). Moving toward the outer layers, it seemed that the arms tended to reorganize themselves around a fixed core; hence, the core is simply more "wrapped" as MW increases, allowing the R_g to remain relatively unchanged within the assemblies. The ξ parameter provides an indication of how the polymer swelling changes upon the distance from the core. The ξ parameters were clearly dependent on the substituent used, and varied in the order: ethyl (**1a,b**) > 3,6-dioxa-8-octane (DOOA) (**1c,d**) > hexyl (**1d**). When combined with the Flory parameter, this provided a consistent picture of how the conformation varies with MW: for larger R_g values the larger core area to cover results in more swollen outer layers and higher ξ values. R_g values varied in the same order as ξ: ethyl > DOOA > hexyl substituents in the BTA core; but, surprisingly, there was no dependence on MW (also see Figure 1e and Figure S29 in the Supporting Information), a key concept for the 3D shape elucidation (Figure 1h).

In summary, aggregation of star-shaped polyglutamates occurred in a nonsalty aqueous environment following polyion concentration dependence with a defined and large CAC together with a fast disassembly upon increasing ionic strength. Lack of spectroscopic features points toward a rather amorphous material with only a recurring characteristic signature involving partial constrain of polyglutamate chains. More importantly, evidence suggested that the self-assembly phenomena proceeded via ionic interactions. These features are characteristic fingerprints of the ubiquitous "ordinary to extraordinary" behavior transition in the dynamics of charged macromolecules in aqueous solutions.[11–13] Although the rational has been controversial for years, there is now a consensus to rationalize the self-assembly of charge-like polyions based on counterion condensation theory. This theory states

that electrostatic potential becomes attractive as the modeled lines of charges approach within the Debye length and the condensed counterions are merged in a shared cloud.[12] Recently, Muthukumar has approached this phenomena collecting reported data over the last decades.[13] Very interestingly, this model predicts a threshold value of a combination of polyion (CAC) and electrolyte concentration (millimolar range) for the transition to the "extraordinary" behavior. Under these conditions, the observed "slow" diffusional mode results from the presence of polyion clusters due to the formation of transient dipoles arising from adsorbed counterions on polyion backbone that can act as physical cross-linking points. This rational is in agreement with the observed behavior on compounds **1a–e**, which displayed a CAC threshold and electrolyte concentration for the self-assembly within the range predicted by Muthukumar. The redshift observed in CD analysis can also be linked to the formation of physical cross-linking dipoles. The fact that we did not observe this behavior for the linear counterparts within the concentrations studied points to the influence of branching, topology, and charge density of compounds **1** that would promote the formation of these cross-linking dipoles.

When compared to reported self-assembled DDS, the architectures generated via "extraordinary" behavior inherently display differential physicochemical features that mediate interactions with biological systems, including size, surface hydrophilicity, charge, lack of internal structure, and enhanced deformability.[23] To assess the biological performance of our new architectures, we aimed to covalently capture our assemblies, as the loose nature of uncaptured assemblies will result in rapid disaggregation in biological media due to increased ionic strength ($\approx 130 \times 10^{-3}$ M) and large dilution rates.[24] Toward this aim, we studied the dynamics, reversibility, and coassembly properties of these systems via stochastic optical reconstruction microscopy (STORM), Förster resonance energy transfer (FRET),[25] and nuclear magnetic resonance (NMR) techniques.

We modified compound **1a** on side chains following well-established methodologies[26] with Cy3 (compound **2c**) and Cy5 (compound **2d**), a FRET pair suitable for STORM microscopy[25,27] (**Figure 2**a and Figure S15–S18 and Table S3 (Supporting Information)). We obtained a concentration-dependent FRET signal when compounds **2c** and **2d** were coassembled, indicating that the two dyes (and therefore the two unimers) were in close proximity within common aggregates (Figure 2b). A key feature of supramolecular aggregates is their dynamic nature, i.e., their ability to continuously assemble and disassemble exchanging monomers. We studied monomer exchange kinetics between preassembled compounds **2c** and **2d** by FRET. Immediately after mixing, a plateau in the signal ratio (and therefore, an equilibrium state) occurred before the first observation time, highlighting the very dynamic nature of our systems.[27] To confirm these indirect spectroscopic observations, we also performed super-resolution STORM experiments for the **2c** and **2d** compounds. Figure 2d demonstrates that all aggregates were single-colored in single component samples (Figure 2d, left); however, both unimers were present within the same nanoassemblies after 2 min of mixing, confirming the rapid monomer exchange observed in FRET studies. Notably, coassembled aggregates of 100–200 nm coexisted with smaller single colored structures, likely to be unimers or low-order
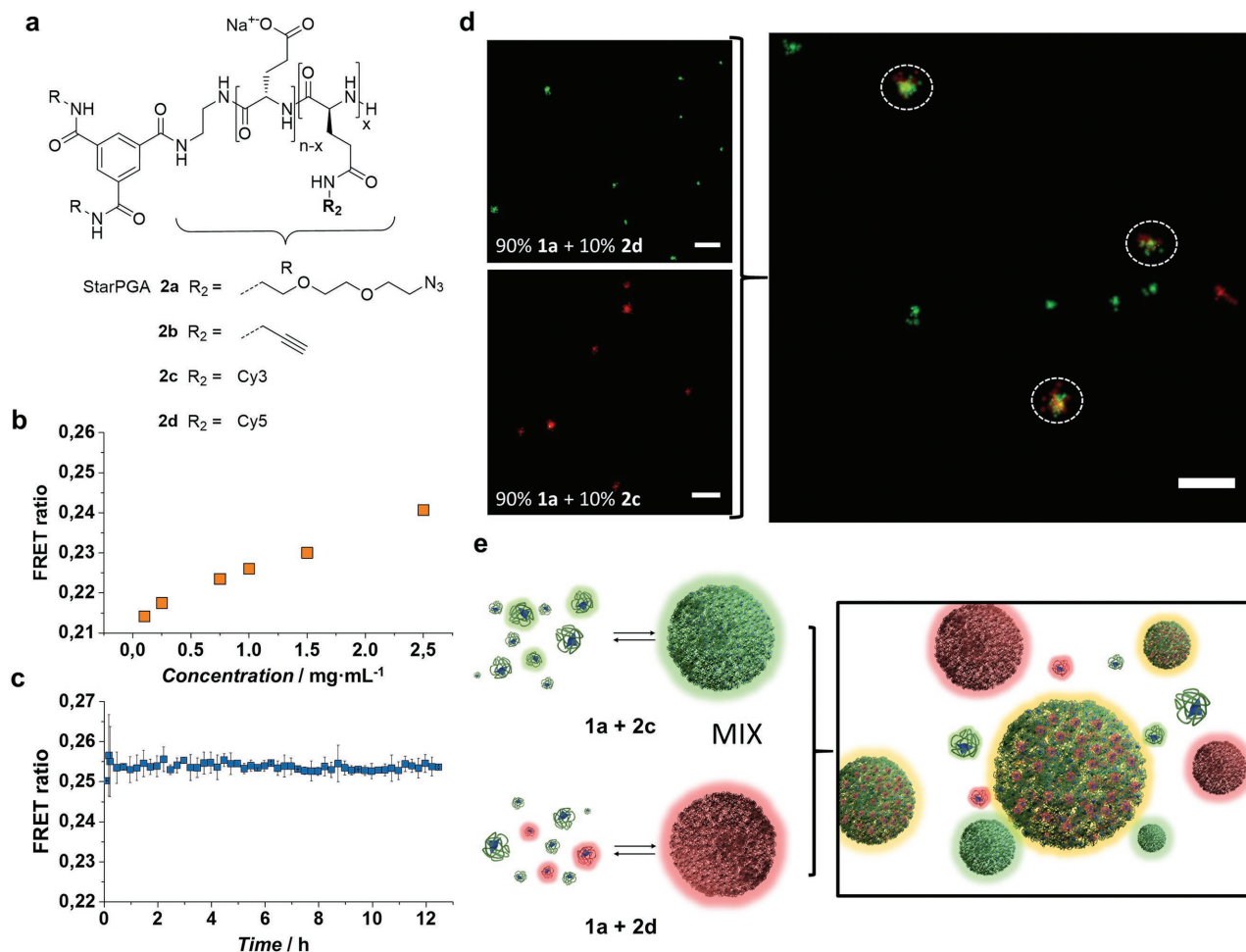
**ADVANCED
SCIENCE NEWS**
www.advancedsciencenews.com

**ADVANCED
MATERIALS**
www.advmat.de

Figure 2. Dynamics and reversibility of the self-assembled star-shaped polyglutamates. a) Star-shaped polyglutamates were fluorescently labeled through postpolymerization modification procedures with Cy3 and Cy5, respectively (see synthetic methods in the Supporting Information). b) FRET ratio reduction upon dilution within nonlabeled compound **1a** (horizontal axis) of fluorescently labeled derivatives (compounds **2d** and **2c**) demonstrates that assembled structures contain both dyes and FRET transfer occurs. c) Mixing of compound **2c** structures (90% **1a** + 10% **2c**) and compound **2d** structures (90% **1a** + 10% **2d**) at a concentration of 2.5 mg mL^{-1} to study their dynamic behavior in time shows small change in FRET ratio. d) STORM images of St–Poly(L-glutamate)(PGA)–Cy3, St–PGA–Cy5, and of the mixture of both structures (2.5 mg mL^{-1}) after 1–2 min of incubation demonstrate a fast dynamic event to the equilibrium state as evidenced by the co-localization of **2c** and **2d** labeled compounds within common aggregates (right panel, dashed lines scale bar 1 μm). e) Schematic illustration of component exchange in the assemblies observed by STORM, confirming the highly dynamic and reversible nature of the self-assembled nanostructures.

oligomers (Figure 2e). Overall, these experiments proved the highly dynamic and reversible nature of the assemblies, evidencing the possibility to build coassembled multifunctional DDS and also stressing the need of stabilization for application in biological environments.

To this end, we modified compound **1a** at the side chain with different degrees of functionalization of azides (compound **2a**) or alkynes (compound **2b**) pursuing a nonreversible covalent stabilization of the assemblies through copper-catalyzed alkyne/azide cycloaddition (CuAAC) (Figure 2a and Figure S12–S14 and Table S2 (Supporting Information)). Although functionalization did not significantly alter the assemblies (up to a 30% molar glutamic acid units substitution, as evidenced by DLS, Figure S37–S40 and Table S8 and S9, Supporting Information), the modification rates for the covalent capture were established as 5% and 10% for

compounds **2a** and **2b**, respectively, displaying sizes similar to model compound **1a** (Figure S30 and S31 and Table S6 and S7, Supporting Information).

We next confirmed the coassembly of compounds **2a** and **2b** by pulsed-field-gradient spin-echo (PFGSE) NMR experiments[28] and determined diffusion coefficients of compounds **1a**, **2a**, and **2b** in D$_2$O above (2 mg mL^{-1}) and below (0.1 mg mL^{-1}) CAC values (**Figure 3**). Diffusion coefficients in the unimeric state (3×10^{-11} m^2 s^{-1}) were found to be one order of magnitude higher than those for aggregated nanoassemblies (4.5×10^{-12} m^2 s^{-1}), indicating R_h values of 6 and 44 nm for unimers and assemblies, respectively, in agreement with DLS data (Figure 3b and Figure S43–S45 (Supporting Information)). We doped a sample containing preassembled compound **2b** with **2a** at a concentration below its CAC. As shown in Figure 3b, the incorporation of **2a** unimers within **2b** nanoassemblies
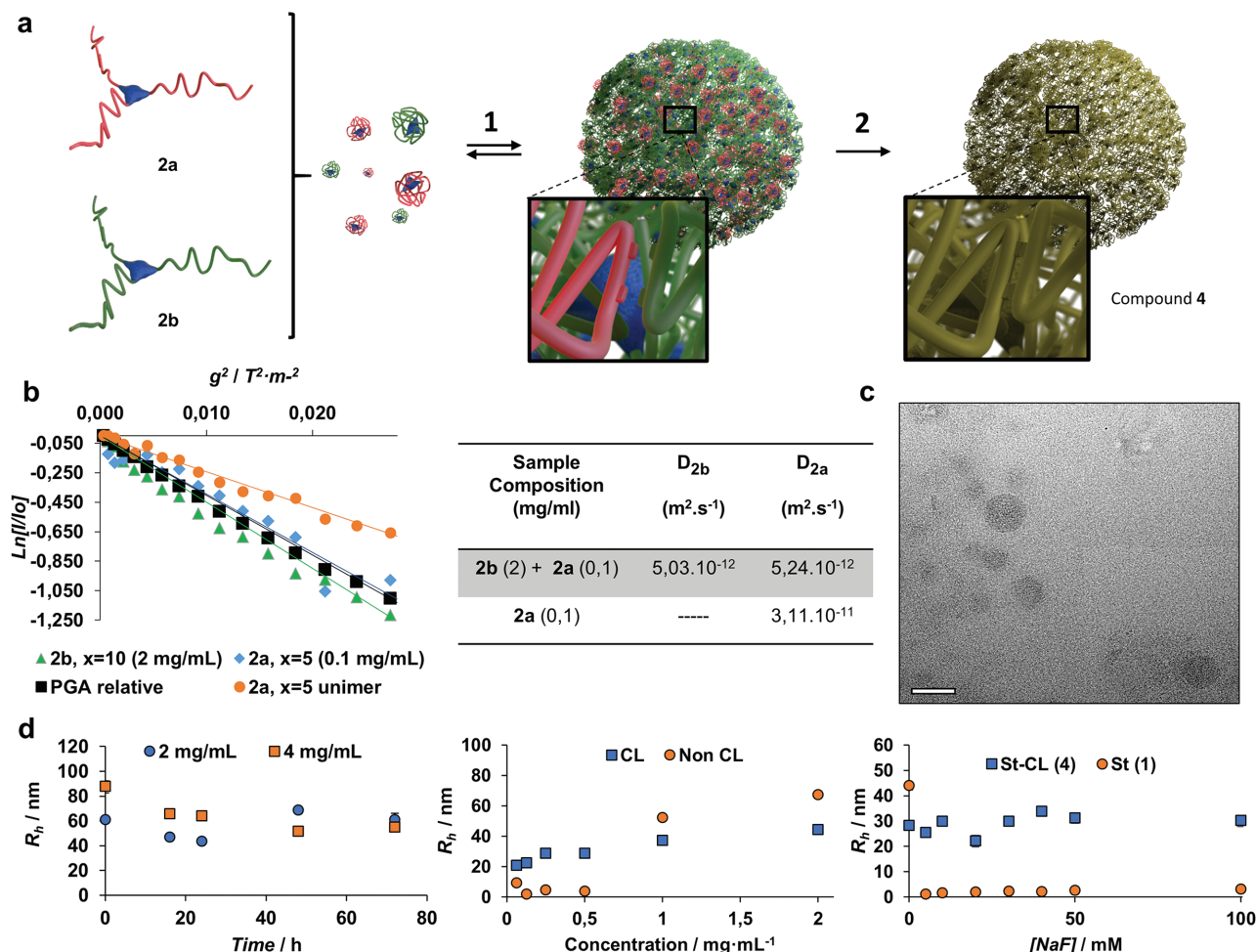
ADVANCED
SCIENCE NEWS
www.advancedsciencenews.com

ADVANCED
MATERIALS
www.advmat.de

Figure 3. Covalent capture strategy toward stable and long circulating delivery systems. a) Coassembly of prefunctionalized and complementary compounds **2a** and **2b** (1) and covalent capture of the coassembled components through azide–alkyne click-chemistry to yield covalently captured compound **4** (2). b) PGFSE-NMR experiments monitored changes in the diffusion coefficient of unimeric compound **2a** (0.1 mg mL^{-1}) in the presence of assembled compound **2b** (2 mg mL^{-1}) (see Figure S43–S45 in the Supporting Information). Analysis shows a reduction in the diffusion coefficient by one order of magnitude of unimeric compound **2a** and indicates the incorporation of these unimers within the assembled compound **2b** nanostructures (table). This provides indirect evidence for the coassembly of these complementary components. c) Cryo-TEM image visualization of covalently captured nanosized compound **4** assemblies (2 mg mL^{-1}, scale bar 50 nm) (also see Figure S25 in the Supporting Information). d) DLS permitted the assessment of assemblies stability along the CuAAC reaction (left panel) and the efficiency of the covalent capture strategy to hinder the reversibility of the system upon dilution (center panel) or increased ionic strength (right panel). Also see, Figure S35 and S36 in the Supporting Information.

was evidenced by the D_f value obtained for **2a** corresponding to self-assembled **2b** ($\approx 5 \times 10^{-12}$ m^2 s^{-1}). We obtained direct proof for spatial proximity through nuclear Overhauser effect spectroscopy (NOESY) NMR experiments where we identified a clear correlation between azide and alkyne motifs (**2a** and **2b**, respectively) (Figure S46, Supporting Information).

Our results point to the feasibility of a covalent capture strategy using CuAAC (Scheme S4 and Figure S19, Supporting Information) and we next monitored assembly stability during coupling conditions (ionic strength $= 2 \times 10^{-3}$ M) of a 1:1 mixture ratio of compounds **2a** and **2b** via DLS (Figure 3d, left). Results showed that after CuAAC reaction, the self-assembled polyglutamates were stable following dilution (with a slight compaction to R_h of 30–40 nm also evidenced by cryo-TEM image shown in Figure 3c) or an increased presence of ionic species. This stability differed from the results found for a physical mixture as

revealed by DLS (Figure 3d) and SANS experiments (Figure S31 and Table S7, Supporting Information). With regard to industrial and clinical concerns, we found the assembly mechanism and covalent capture strategy to be highly robust and reproducible (Figure S37–S41 and Table S8 and S9, Supporting Information). The covalent capture of dynamic assemblies is a highly attractive proposition, as they have the potential to be applied in novel DDS strategies containing unique features that could yield advantageous biological consequences.

We labeled compound **4** with fluorescence dyes to monitor in vitro and in vivo performance (**Figure 4**), yielding compounds **5a** (bearing Oregon Green, for live-cell imaging, see the Supporting Information) and **5b** (with Cy5.5, for in vivo imaging). Importantly, surface modification of compound **4** did not induce structural changes in the parental structure (Figure 4a,b and Figure S34 and S38 and Table S8 and S9
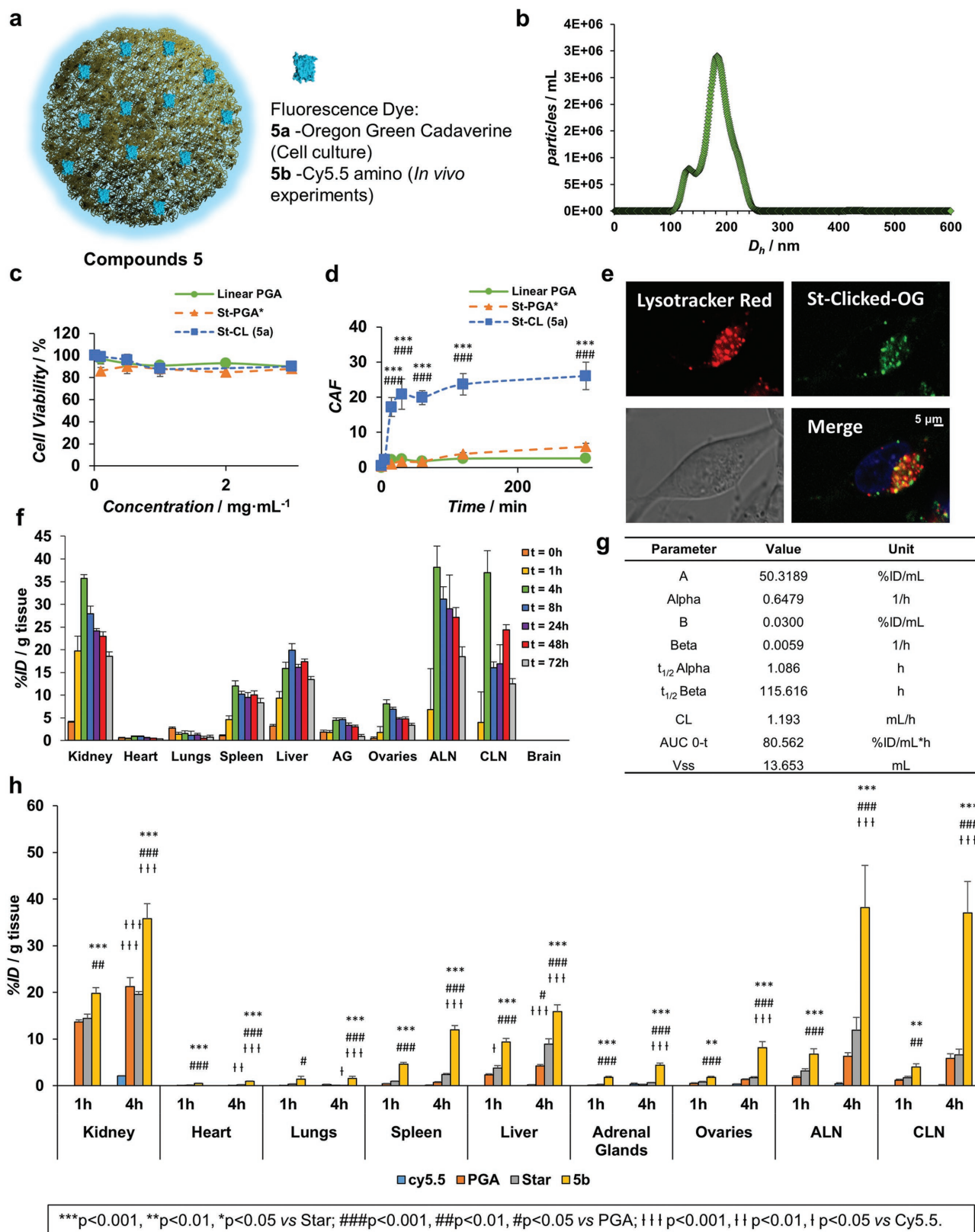
Compounds 5

Fluorescence Dye:
5a -Oregon Green Cadaverine (Cell culture)
5b -Cy5.5 amino (*In vivo* experiments)

Parameter	Value	Unit
A	50.3189	%ID/mL
Alpha	0.6479	1/h
B	0.0300	%ID/mL
Beta	0.0059	1/h
$t_{1/2}$ Alpha	1.086	h
$t_{1/2}$ Beta	115.616	h
CL	1.193	mL/h
AUC 0-t	80.562	%ID/mL*h
Vss	13.653	mL

***$p<0.001$, **$p<0.01$, *$p<0.05$ *vs* Star; ###$p<0.001$, ##$p<0.01$, #$p<0.05$ *vs* PGA; †††$p<0.001$, ††$p<0.01$, †$p<0.05$ *vs* Cy5.5.

Figure 4. Biological validation of the covalently captured nanostructures as drug delivery systems. a) Schematic representation of the surface modification of compound **4** with fluorescence dyes. b) Nanoparticle Tracking Analysis (NTA) in ddH₂O shows particle distribution of compound **5b** in agreement with DLS and Cryo-TEM. c) SHSY5Y cell viability by MTS assay in response to compound **4** (72 h) demonstrated lack of toxicity (*n* > 3, mean ± SEM). d) Cell-associated

**ADVANCED
SCIENCE NEWS**
www.advancedsciencenews.com

**ADVANCED
MATERIALS**
www.advmat.de

(Supporting Information)). Cell viability assays using SHSY5Y neuroblastoma cells as model cancer cell line and human fibroblasts derived from new-born foreskin as a normal cell model revealed absence of cell toxicity up to the concentrations tested, (see Figure S48 in the Supporting Information), suggesting the feasibility of the CuAAC strategy after proper Cu removal (Figure 4c). A lack of toxic side effects was also demonstrated via histological analysis of tissue slices of key organs extracted from **5b**-treated animals at 24 and 72 h postinjection (Figure S53, Supporting Information).

As expected for macromolecular systems of such origin,[29] an energy-dependent uptake was observed (Figure 4d) with a clear co-localization of compound **5a** with LysoTracker Red indicating the suitability of these nanocarriers for lysosomotropic drug delivery[30] (Figure 4e). Importantly, in neuroblastoma cells, a significantly enhanced in vitro cell internalization rate for compound **5a** when compared with linear-polyglutamate and star unimer (**1a**), was demonstrated by flow cytometry and live-cell confocal microscopy, probably due to the larger size and greater negative z-potential (Figure S49 and S50, Supporting Information).[31] In vivo biodistribution of **5b** in healthy mice revealed renal excretion profiles, as observed for other polyglutamates.[15] Larger accumulation in all organs generally occurred for **5b** and, importantly, we also observed significantly greater terminal and accumulation half-life for **5b** ($t_{1/2}$ beta 115.6 h and $t_{1/2}$ alpha 1.1 h) when compared to the linear (0.6 and 0.10 h) or star unimer (**1a**) counterparts (12 and 0.15 h), respectively (Figure S51 and S52 and Table S11, Supporting Information).[15] Increased half-life may enhance passive targeting by the EPR effect when used in well-vascularized solid tumors or inflamed areas[4] (Figure 4f,g).

Remarkably, we observed a clear accumulation of compound **5b** in immune system-related organs including the spleen and lymph nodes (axillary (ALN) and cervical (CLN)) (Figure 4h, $p < 0.001$), highlighting the great potential of our stabilized self-assemblies as carriers to target lymph node metastasis, cancer immunotherapy, or immune system-related approaches, such as vaccination after the adequate conjugation of antigens or adjuvants.[32,33] The preferential internalization by macrophages and other immune-system related cells of the polyglutamate-based nanocarriers as already seen clinically[34] together with **5b** intrinsic physicochemical properties may contribute to such behavior. Indeed, the inherent structural and morphological features of these soft materials, such as their size range ($\approx$100 nm), highly negative z-potential values, and/or hydrophilic surfaces, represent key features for lymph node targeting.[32,35,36] Our findings are of special interest given that we obtained up to 40% injected dose per gram tissue **5b** accumulation in the lymph nodes after intravenous administration. Although a direct comparison would not be rigorous given the large heterogeneity in the animal models and techniques employed for quantification

in literature, this accumulation value stands among the maximum reported values in literature so far, and could even be enhanced by employing subcutaneously administration.[35,37] These data demonstrate the applicability of our self-assembled polyglutamates as lymphotropic delivery vehicles, opening up a vast range of therapeutic approaches.

Within this study, we have provided a simple yet efficient bottom-up approach for the design of long circulating nanocarriers, taking advantage, for the first time, of the "extraordinary" behavior identified for star-shaped polyglutamates in nonsalty aqueous solutions. In our attempts to construct advanced nanosized carriers based on star-shaped polyglutamates, we identified a charge-like self-assembly phenomena for electrostatically repulsive macromolecules that may represent a paradigm shift for conventional nanocarrier design. A thorough study employing a wide battery of instrumental techniques allowed us to rationalize these observations under the so-called "ordinary to extraordinary" transition behavior. We noted that under low ionic strength ($<10 \times 10^{-3}$ M), these charged macromolecules experience an unexpected self-assembly process, yielding spherical objects in the range of 30–100 nm in radius, a highly negative z-potential with a highly dynamic equilibrium, and a rapid disassembly upon an effective charge screening. This self-assembly mechanism was found to be driven by ionic interactions following a recently reported model, where the adsorbed counterions are shared in a merged cloud creating transient dipoles in the polyanionic backbone that can act as cross-linking points. We constructed these biodegradable and biocompatible self-assembled cross-linked star-shaped polyglutamates using a reproducible and scalable bottom-up methodology followed by a covalent stabilization. This strategy enabled in vitro and in vivo evaluation, revealing a lack of toxicity, an enhanced in vitro cell internalization rate, and significantly greater terminal and accumulation half-life in vivo. These results allow us to envisage these systems as promising nanocarriers for therapeutic or diagnostic applications, especially in anticancer treatments. Additionally, further studies to identify the mechanism for the significant accumulation found in the lymph nodes will open up a wide range of opportunities for the currently unsuccessful clinical approaches to target lymph node metastasis, imaging of sentinel lymph nodes, and cancer immunotherapy.

Experimental Section

Synthesis of Star-Shaped Poly(L-glutamates): Detailed synthetic methodologies and full characterization of the initiators, monomers, polymerizations, deprotection steps, postpolymerization modifications, and covalent capture strategies are fully described in the Section "Synthetic Procedures" in the Supporting information.

DLS: DLS measurements were performed using a Malvern ZetasizerNanoZS instrument, equipped with a 532 nm laser at a fixed scattering angle of 173°. Solutions were sonicated for 10 min and

---

fluorescence (CAF) over time of the energy-dependent uptake (experiment at 37–4 °C to exclude binding) shows a significant increase for compound **5a** ($n > 3$, mean ± SEM). e) Confocal image of compound **5a** uptake at 2 h post-treatment in SHSY5Y cells following a pulse–chase experiment (Blue-Hoechst 33342 for nuclei; Green-Oregon-green for compound **5a**; Red-LysoTracker Red). Colocalization with LysoTracker marker was observed (yellow). f) In vivo biodistribution after intravenous injection of compound **5b** shows renal excretion profiles with accumulation in lymph nodes. Data expressed as normalized % injected dose (ID) per gram of tissue ($n > 5$, mean ± SEM). g) Pharmacokinetic parameters obtained from compound **5b** plasmatic profiles. h) In vivo biodistribution of compound **5b** toward **1a** and linear PGA at 1 and 4 h postinjection confirms the clear significantly higher accumulation of **5b** in spleen and lymph nodes (axillary, ALN and cervical, CLN). Data expressed as normalized % injected dose (ID) per gram of tissue ($n > 5$, mean ± standard error of the mean (SEM)).

**ADVANCED
SCIENCE NEWS** _____

www.advancedsciencenews.com

**ADVANCED
MATERIALS**

www.advmat.de

allowed to age for the required time, filtered through a 0.45 µm cellulose membrane filter, and measured. Size distribution was measured (radius, nm) for each polymer in triplicate with $n > 3$ measurements.

For size measurements, polymer solutions were prepared under different conditions (double-deionized water, ddH$_2$O, phosphate buffers, or salt containing solutions at different concentrations and temperatures). Automatic optimization of beam focusing and attenuation was applied for each sample. CAC was determined using a previously described method.[17]

TEM Images: TEM images were recorded using a JEOL 2100 transmission electron microscope. Samples of polyglutamates were applied directly onto carbon film on 200 mesh copper grids. Excess of sample was carefully removed by capillarity, and the grids were immediately stained with one drop of 0.1% phosphotungstic acid for 30 s. Excess stain was removed by capillary action.

Cryo-TEM Tomography: In order to achieve the 3D characterization of star-shaped self-assembled systems, a series of different electron tomograms was obtained. The sample was incubated in Quantifoil R3.5/1 holey carbon copper grids and vitrified using standard procedures with a Vitrobot (FEI). The samples included 10 nm gold nanoparticles (as fiducial markers) used in alignment process. Vitrified grids were transferred into a 914 high tilt cryo transfer tomography holder (Gatan Inc.) and analyzed on a JEM-2200FS/CR (JEOL, Ltd.) field emission gun electron microscope, operating at 200 kV at nitrogen liquid temperature. Single-axis tomographic tilt series were collected under low-dose conditions on a 4k × 4k UltraScan 4000 charged-coupled device (CCD) camera (Gatan Inc.), over a tilt range of ±64° with 2° increments and at underfocus values ranging from 5 to 8 mm, using the semiautomatic data acquisition software SerialEM. Different tilt series at a nominal magnification of 30 000, producing a final pixel size of 0.71 nm, were collected with SerialEM in low-dose mode. The in-column Omega energy filter helped to record images with improved signal-to-noise ratio by zero-loss filtering with an energy slit width of 30 eV centered at the zero-loss peak. The total dose used for a tilt series was 90–100 electrons A$^{\circ -2}$.[38]

Tomographic Reconstruction: For alignment and 3D reconstruction of the tilted series, IMOD software was used. 10 nm gold particles were used as fiducial markers during alignment, and 3D reconstruction was carried out by weight back-projection. No contrast transfer function (CTF) correction was applied, thus limiting the reconstructions to the first zero of the CTF.[39]

SANS: SANS experiments were performed using the D11 diffractometer at the Institute Laue–Langevin (ILL, Grenoble), and diffractometers SANS2d and LOQ at the ISIS Spallation Neutron Source (Didcot, UK). All solutions were prepared in D$_2$O at concentrations of 1–0.01 wt% and were placed in 2 mm path length, UV-spectrophotometer grade, quartz cuvettes (Hellma UK) and mounted in aluminum holders on top of an enclosed, computer-controlled, sample chamber. Sample volumes were ≈0.6 cm^3. Temperature control was achieved using a thermostated circulating bath pumping fluid through the base of the sample chamber, achieving a temperature stability of ±2 °C. Data were collected and corrected for the scattering and transmission of the solvent and cell and were placed on an absolute intensity scale with reference to a flat scatterer. Scattering data are expressed in terms of the scattering vector Q which is given by $Q = 4n\pi/\lambda \sin(\theta/2)$ in which n is the refractive index for neutrons ($n \approx 1$), λ is the wavelength, and θ is the scattering angle. Data were corrected for transmission intensity, electronic background and normalized against a flat scatter according to standard procedures for the instrument. The obtained scattering profiles $I(Q)$ versus Q were analyzed according to $I(Q) \propto \Phi V_p P(Q) S(Q) + B_{inc}$ where Φ is the volume fraction and V_p the particle volume. B_{inc} is the incoherent scattering, generally dominated by the protons present in the sample, which usually depends on the concentration of polymer. The FISH modeling suite was used for the analysis.[40] FISH incorporates parameterized form factors, $P(Q)$ and structure factors, $S(Q)$, to describe the dimensions of the scattering particle and interparticle interaction.

FRET: Unimer stock solutions of compounds **1a**, **2d**, and **2c** at a concentration of 0.25 mg mL^{-1} were prepared. For dilution experiments, the stock samples were mixed in a ratio of 80/10/10 **1a**/**2d**/**2c**; while for dynamic experiments, stock solutions were mixed to obtain 10% **2c** or **2d**/**1a**. Samples were lyophilized, suspended in ddH$_2$O water at a concentration of 2.5 mg mL^{-1}, and left to equilibrate for 24 h before measurement to ensure nanoassembly formation. To perform FRET experiments, the samples were excited at a wavelength of 500 nm and the emission profile was collected from 545 to 800 nm using a Tecan infinite M200 Pro Microplate reader. The emission fluorescence of Cy5 (at 647 nm) was divided by the emission fluorescence of the Cy3 (561 nm) to obtain FRET ratios.

Nanosight Measurements: Nanoparticle tracking analysis was performed on a NS300 apparatus equipped with a complementary metal-oxide-semiconductor (CMOS) camera mounted on an optical microscope to track scattered light by particles illuminated a focused (80 µm) beam generated by a single mode laser diode (488 nm). This technique combines a conventional optical microscope with a laser light source to illuminate nanoscale particles within the sample (mL) introduced to the viewing unit with a disposable syringe. Laser light illuminates particles in suspension and a video camera captures the scattered light produced. Particle diffusion was determined by tracking individual particle positional changes in two dimensions, from which hydrodynamic diameter could then be determined for each particle, thereby providing direct measurement on size and particle counts. Particles were tracked using the built-in software for 60 s at 30 fps at 25 °C. The particle sizes and concentrations were evaluated employing the Nanoparticle Tracking Analysis (NTA) software, data are represented as mean hydrodynamic diameter and particles per mL.

STORM: To perform direct STORM imaging, star-shaped poly(L-glutamates) were immobilized by adsorption onto the surface of a flow chamber assembled from a glass slide and a coverslip (24 mm × 24 mm, thickness 0.15 mm) separated by double-sided tape. After being incubated for 10–15 min, unbound structures were removed by washing the chamber twice with STORM buffer. STORM buffer contains phosphate buffer saline (PBS), an oxygen scavenging system (0.5 mg mL^{-1} glucose oxidase, 40 µg mL^{-1} catalase), 5% (w/v) glucose, and 100×10^{-3} M cysteamine.

STORM images were acquired using a Nikon N-STORM system configured for total internal reflection fluorescence imaging. Compound **2d** was imaged by means of a 647 nm laser (160 mW) and compound **2c** was imaged by means of a 488 nm laser (80 mW). No activation of UV light was employed. Fluorescence was collected by means of a Nikon 100×, 1.49 numerical aperture (NA) oil-immersion objective and passed through a quad-bandpass dichroic filter (97335 Nikon). Images were acquired onto a 256 × 256 pixel region (pixel size 0.16 µm) of a Hamamatsu ORCA- Flash 4.0 camera at 10 ms integration time. STORM images were analyzed with the STORM module of the NIS element Nikon software. The NIS element Nikon software generates a list of localizations by Gaussian fitting of blinking dyes in the acquired movie of conventional microscopic images. This analysis takes around 2 min per image, and can be run in a batch mode. To avoid overcounting, blinking detected in consecutive frames are counted as single by the software.

NMR Experiments: NMR spectra were recorded at 27 °C (300 K) on an Avance III 500 MHz Bruker spectrometer equipped with a 5 mm TBI broadband probe or a 300 Ultrashield from Bruker (Billerica, MA, USA). Data were processed with the software Mestrenova (Bruker GmbH, Karlsruhe, Germany). Samples were prepared at the desired concentration in D$_2$O.

Diffusion Experiments (500 MHz): Pulsed-field-gradient NMR spectroscopy was used to measure translational diffusion by fitting the integrals or intensities of the NMR signals to the Stejskal–Tanner[41] equation: $I = I_0 \exp[-D\gamma^2 g^2 \delta^2 (\Delta - \delta\delta 3)]$ where I is the observed intensity, I_0 the reference intensity (unattenuated signal intensity), D the diffusion coefficient, γ the gyromagnetic ratio of the observed nucleus, g the gradient strength, δ the length of the gradient, and Δ the diffusion time. 2D diffusion-ordered NMR spectroscopy was performed with a stimulated echo sequence using bipolar gradient pulses. The lengths of delays were held constant at $\Delta = 10$ ms, and 32 spectra of 64 scans

each were acquired with the strength of the diffusion gradient varying between 5% and 95%. The lengths of the diffusion gradient and the stimulated echo were optimized for each sample. Typical values were $\delta = 1.5$ ms for the analysis of nonaggregated species (0.1 mg mL^{-1}) and 5 ms to study the nanoassemblies.

NOE Experiments (500 MHz): 2D NOE experiments (NOESY) where recorded with a mixing time of 100 ms with 128 scans.

Cell-Culture Protocols: SHSY5Y cells from ATCC were cultured in Dulbecco's modified Eagle medium (DMEM) media supplemented with fetal bovine serum. Cells were maintained at 37 °C in an atmosphere of 5% carbon dioxide and 95% air. Medium was replaced every 2–3 d and underwent passage once weekly when 80% of cell confluence was reached.

MTS Assay for Cell Viability: Cells were seeded in sterile 96-well microtiter plates at a cell density of 35 000 cells cm^{-2} for SHSY5Y. Plates were incubated for 24 h and compounds (0.2 µm filter sterilized) were then added to give a final concentration of 0–3 mg mL^{-1}. After 72 h of incubation, (3-(4,5-dimethylthiazol-2-yl)-5- (3-carboxymethoxyphenyl)-2- (4-sulfophenyl)-2H-tetrazolium) (MTS)/phenazine methosulfate (PMS) (20:1) (10 µL of manufacturer solution) was added to each well, and the cells were incubated for a further 2 h. Optical density of each well was measured at 490 nm spectrophotometrically using Victor^{2}Wallac plate reader. The absorbance values were represented as the percentage of cell viability taken as 100% cell viability of untreated control cells.

Cellular Uptake by Flow Cytometry of Oregon Green-Labeled Polymers in SHSY5Y Cells: SHSY5Y cells were seeded in 6-well plates at a density of 35 000 cells cm^{-2} (1 mL cell suspension per well) and allowed to adhere for 24 h. In binding experiments conducted at 4 °C, cells were preincubated at this temperature for 30 min prior to starting the experiment. For both experiments, 4 and 37 °C, the cathepsin B inhibitor CA-074 (0.4 µL from a solution of 5×10^{-6} M to reach a final concentration of 2×10^{-6} M) was added 30 min before the addition of the conjugate. Then, 10 µL of Oregon Green (OG)-labeled polymer (0.01 mg OG per mL) was added at different time points from 0 to 300 min while cells were incubated either at 37 or 4 °C for each experiment. Finally, cells were placed on ice to inhibit energy dependent mechanisms and washed twice with cold PBS–BSA 0.1%. (PBS supplemented with bovine serum albumin (BSA)). Then, cells were resuspended in 0.5 mL of cold PBS using a cell scraper. Finally, the cell pellet was placed in flow cytometer tubes. Cell-associated fluorescence (CAF) was then analyzed using a Becton Dickinson fluorescence-activated cell sorting FACSCalibur cytometer (California, USA) equipped with an argon laser (488 nm) and emission filter for 550 nm. Data collection involved 10 000 counts per sample, and data were analyzed using CELLQuest version 3.3 software. Data are expressed by plotting the CAF, which is the result of the % of positive cells multiplied by the mean fluorescence (CAF = % positive cells × mean fluorescence/100). Cells incubated without polymer were used to account for the background fluorescence.

Statistical Analysis: Data from the experiments were analyzed using one-way analysis of variance (ANOVA). In all cases, differences were considered to be significant when ***$p < 0.001$; **$p < 0.01$; *$p < 0.05$; ns: nonsignificant.

Confocal Fluorescence Microscopy—Live-Cell Imaging: For live-cell imaging, SHSY5Y cells were seeded at a density of 35 000 cells cm^{-2}, on glass bottom culture dishes (1 cm^2 Petri plate) and allowed to seed for 24 h at 37 °C. The experiment was performed following a pulse–chase mode at 37 °C. First, the cathepsin B inhibitor CA-074 (0.4 µL from a solution of 5×10^{-6} M to reach a final concentration of 2×10^{-6} M) was added 30 min prior the addition of the St–PGA–OG. Then, 10 µL of OG-labeled polymer (0.01 mg OG per mL) was added and the cells were incubated for 2 h at 37 °C (pulse). The medium was removed and cells were washed twice with PBS. 1 mL of medium containing 2×10^{-6} M of the CA-074 inhibitor was then added, and cells were incubated for 4 h at 37 °C (chase). 30 min before washing the cells with PBS–BSA 0.1%, the nuclear marker Hoechst (1 µL from a solution of 5×10^{-6} M) and the lysosomal marker LysoTracker Red (0.75 µL from a solution of 100×10^{-6} M) were added and incubated for 20 min in order to identify possible co-localizations and therefore establish an endocytic pathway. Finally, cells were washed

with PBS–BSA 0.1%. Then, the glass was removed and placed on the microscope chamber with fresh media containing 2×10^{-6} M of CA-074 inhibitor. Samples were analyzed under the microscope. Images were captured with an inverted DM IRE2 microscope equipped with a λ-blue 60× oil immersion objective and handled with a TCS SP2 system, equipped with an acoustic optical beam splitter. Excitation was performed with an argon laser (OG 496 nm), HeNe laser (LysoTracker Red 594 nm), and blue diode (Hoechst 405 nm). Images were captured at an 8-bit gray scale and processed with Leica Confocal Software (LCS) (version 2.5.1347a, Leica Germany) containing multicolor, macro-, and 3D components. Control cells that followed the same incubation time were also analyzed to establish the autofluorescence, as well as cells treated only with Hoechst or LysoTracker Red.

Biodistribution Experiment and Fluorescence Quantification: Biodistribution experiments were carried out using female athymic nude mice of five to seven weeks from Envigo. Animals were housed on a 12 h light and 12 h dark cycle. Water and food was provided ad libitum during the whole experiments in all cases, and general aspect, behavior, and body weight were evaluated daily to ensure animal wellness. All animal protocols were approved by the Institutional Animal Care and Use Committee at the Centro de Investigación Príncipe Felipe (Valencia, Spain). For the pharmacokinetics and biodistribution study, 30 mice were used (five mice at each time point, 25 ± 4.5 g of body weight). The labeled polymer was administered intravenously through the tail vein at a dose of 4.15 mg kg^{-1} Cy5.5 eq. (5.41 mg mL^{-1} polymer) in serum saline. Mice were euthanized at 0, 4, 8, 24, 48, and 72 h postadministration. Blood, major organs (heart, lungs, spleen, liver, kidneys, and brain), and small organs (ovaries, adrenal glands, axillary and cervical lymph nodes) were harvested after flushing with 10 mL PBS. Then, organs were weighted and stored at −80 °C for subsequent homogenation and fluorescence quantification. Blood samples were centrifuged immediately after extraction (10 min, 4000 rpm, 4 °C) and plasma (supernatant) and pellet were stored separately at −80 °C. For fluorescence quantification, major organs and fallopian tube were homogenized in Dulbecco's phosphate buffered-saline (DPBS) pH = 7.4 at a specific concentration by means of Ultraturrax device and the rest of the small organs were homogenized manually with a potter glass (see Table S5 in the Supporting Information). Suspensions obtained were centrifuged (4000 rpm, 1 h, 4 °C) and supernatants were collected for fluorescence measurement. Supernatants of organs collected and plasma were measured (100 µL) per triplicate in 96 well-plates using Victor^{2}Wallace by fluorescence (595 nm excitation and 680 nm emission). To relate the fluorescence with the concentration of conjugate present in the organ, a calibration curve was previously performed.

Statistical Analysis: Data from the experiments were analyzed using one-way ANOVA and Bonferroni posthoc for pairwise comparison. In all cases, differences were considered to be significant with ***$p < 0.001$; **$p < 0.01$; *$p < 0.05$; ns: nonsignificant. ***$p < 0.001$ **5b** versus star, ###$p < 0.001$ **5b** versus PGA, t t t$p < 0.001$ **5b** versus Cy5.5.

Pharmacokinetics: The data analysis was performed by nonlinear regression using the SOLVER function of the spreadsheet program Microsoft Excel as has been described by Martin et al.[42] (the pharmacokinetic parameters were A, B, ALPHA, and BETA). From these parameters, several derived pharmacokinetic parameters were computed: AUC ($A/ALPHA + B/BETA$), CL (D/AUC), V_{ss}, C_{max} ($A + B$), and apparent terminal half-life. As plasma concentrations often span a wide range, it is useful to employ a weighting procedure for the raw data that allows one to fit low concentrations and high concentrations simultaneously. Weighting by the deviation standard of the concentration was used: Weighting: $1/Y^2$.

Histology: Key organs for the determination of the absence of toxicity after **5b** administration to mice were extracted from euthanized animals at 24 and 72 h biodistribution time points. After being washed with PBS, kidneys, livers, and spleen were fixed in paraformaldehyde (PFA) for 24 h. Then, the excess of PFA was removed by washing with PBS under strong agitation (200 rpm) for 20 min, five times. Finally, samples were stored in a solution of PBS with 0.05% of sodium azide. In order to include the sample in paraffin, a previous dehydration of the sample through 2 min incubation in increased degree of alcohol solutions (30%, 50%, 70%, 96%, and 99.9%) was performed, followed by two xylol washes of 1 min

**ADVANCED
SCIENCE NEWS**

www.advancedsciencenews.com

**ADVANCED
MATERIALS**

www.advmat.de

to finally include the sample in paraffin. Then, the paraffin block was cut in 5 µm slide and set up in SuperFrost plus glass slide to hematoxylin–eosin staining. For hematoxylin–eosin staining, previous tissue slides were deparaffinized with xylene and then rehydrated with a decreasing battery of ethanol solutions (99.9%, 96%, 70%) and water (5 min) followed by Dako hematoxylin staining for 2.5 min. Tissue samples were then washed with deionized water (1.5 min bath), blueing buffer (1 min), and water (1.5 min). Then, tissue slides were incubated 2 min in lithium carbonate and HCl 0.25% in ethanol 70% in order remove the excess of hematoxylin staining. Following that, tissue slides were incubated with Dako eosin for 2 min. Finally, dehydration was performed by washing with 96% ethanol (30 s) and 99.9% ethanol (2.5 min). The slide was then mounted with Eukitt.

Supporting Information

Acknowledgements

Conflict of Interest

ADC, VJN, and MJV declare that a patent with reference WO2017025298A1 has been filed related to the present work.

Keywords

[1] a) J. I. Hare, T. Lammers, M. B. Ashford, S. Puri, G. Storm, S. T. Barry, *Adv. Drug Delivery Rev.* **2017**, *108*, 25; b) J. Shi, P. W. Kantoff, R. Wooster, O. C. Farokhzad, *Nat. Rev. Cancer* **2017**, *17*, 20.

[2] a) H. E. Gendelman, V. Anantharam, T. Bronich, S. Ghaisas, H. Jin, A. G. Kanthasamy, X. Liu, J. McMillan, R. L. Mosley, B. Narasimhan, S. K. Mallapragada, *Nanomedicine* **2015**, *11*, 751; b) M. Goldsmith, L. Abramovitz, D. Peer, *ACS Nano* **2014**, *8*, 1958; c) J. A. Jackman, J. Lee, N.-J. Cho, *Small* **2016**, *12*, 1133.

[3] a) R. Duncan, *J. Controlled Release* **2014**, *190*, 371; b) A. C. Anselmo, S. Mitragotri, *Bioeng. Transl. Med.* **2016**, *1*, 10.

[4] a) H. Maeda, K. Tsukigawa, J. Fang, *Microcirculation* **2016**, *23*, 173; b) H. Maeda, H. Nakamura, J. Fang, *Adv. Drug Delivery Rev.* **2013**, *65*, 71.

[5] a) D. G. Rudmann, J. T. Alston, J. C. Hanson, S. Heidel, *Toxicol. Pathol.* **2013**, *41*, 970; b) Y. Wang, A. Santos, A. Evdokiou, D. Losic, *J. Mater. Chem. B* **2015**, *3*, 7153.

[6] a) A. Duro-Castano, I. Conejos-Sanchez, M. J. Vicent, *Polymers* **2014**, *6*, 515; b) O. Zagorodko, J. J. Arroyo-Crespo, V. J. Nebot, M. J. Vicent, *Macromol. Biosci.* **2017**, *17*, 1600316.

[7] a) I. N. Kurniasih, J. Keilitz, R. Haag, *Chem. Soc. Rev.* **2015**, *44*, 4145; b) A. Duro-Castano, J. Movellan, M. J. Vicent, *Biomater. Sci.* **2015**, *3*, 1321.

[8] a) P. Mi, D. Kokuryo, H. Cabral, H. Wu, Y. Terada, T. Saga, I. Aoki, N. Nishiyama, K. Kataoka, *Nat. Nanotechnol.* **2016**, *11*, 724; b) C. V. Synatschke, T. Nomoto, H. Cabral, M. Foertsch, K. Toh, Y. Matsumoto, K. Miyazaki, A. Hanisch, F. H. Schacher, A. Kishimura, N. Nishiyama, A. H. E. Mueller, K. Kataoka, *ACS Nano* **2014**, *8*, 1161; c) Y. Anraku, A. Kishimura, Y. Yamasaki, K. Kataoka, *J. Am. Chem. Soc.* **2013**, *135*, 1423; d) G. J. Weiss, J. Chao, J. D. Neidhart, R. K. Ramanathan, D. Bassett, J. A. Neidhart, C. H. J. Choi, W. Chow, V. Chung, S. J. Forman, *Invest. New Drugs* **2013**, *31*, 986; e) W. Wu, W. Wang, J. Li, *Prog. Polym. Sci.* **2015**, *46*, 55; f) A. Joseph, C. Contini, D. Cecchin, S. Nyberg, L. Ruiz-Perez, J. Gaitzsch, G. Fullstone, J. Azizi, J. Preston, G. Volpe, G. Battaglia, *bioRxiv* **2016**, DOI: 10.1101/061325.

[9] a) J. C. Butler, T. Angelini, J. X. Tang, G. C. L. Wong, *Phys. Rev. Lett.* **2003**, *91*, 028301; b) A. Diehl, H. A. Carmona, Y. Levin, *Phys. Rev. E* **2001**, *64*, 011804.

[10] a) L. J. Gagliardi, *J. Biophys* **2013**, *3*, 133; b) J. X. Tang, P. A. Janmey, *J. Biol. Chem.* **1996**, *271*, 8556; c) O. Lambert, L. Letellier, W. M. Gelbart, J. L. Rigaud, *Proc. Natl. Acad. Sci. USA* **2000**, *97*, 7248.

[11] J. M. Schurr, K. S. Schmitz, *Annu. Rev. Phys. Chem.* **1986**, *37*, 271.

[12] G. S. Manning, J. Ray, *J. Biomol. Struct. Dyn.* **1998**, *16*, 461.

[13] M. Muthukumar, *Proc. Natl. Acad. Sci. USA* **2016**, *113*, 12627.

[14] J. Li, T. Ngai, C. Wu, *Polym. J.* **2010**, *42*, 609.

[15] A. Duro-Castano, R. M. England, D. Razola, E. Romero, M. Oteo-Vives, M. Angel Morcillo, M. J. Vicent, *Mol. Pharmaceutics* **2015**, *12*, 3639.

[16] R. Holm, B. Weber, P. Heller, K. Klinker, D. Westmeier, D. Docter, R. H. Stauber, M. Barz, *Macromol. Biosci.* **2017**, *17*, 1600514.

[17] M. Khuphe, A. Kazlauciunas, M. Huscroft, P. D. Thornton, *Chem. Commun.* **2015**, *51*, 1520.

[18] S. Cantekin, T. F. A. de Greef, A. R. A. Palmans, *Chem. Soc. Rev.* **2012**, *41*, 6125.

[19] a) M. A. J. Gillissen, M. M. E. Koenigs, J. J. H. Spiering, J. A. J. M. Vekemans, A. R. A. Palmans, I. K. Voets, E. W. Meijer, *J. Am. Chem. Soc.* **2014**, *136*, 336; b) C. M. A. Leenders, M. B. Baker, I. A. B. Pijpers, R. P. M. Lafleur, L. Albertazzi, A. R. A. Palmans, E. W. Meijer, *Soft Matter* **2016**, *12*, 2887.

[20] a) I. de Feijter, P. Besenius, L. Albertazzi, E. W. Meijer, A. R. A. Palmans, I. K. Voets, *Soft Matter* **2013**, *9*, 10025; b) C. M. A. Leenders, L. Albertazzi, T. Mes, M. M. E. Koenigs, A. R. A. Palmans, E. W. Meijer, *Chem. Commun.* **2013**, *49*, 1963.

[21] P. Lo Nostro, B. W. Ninham, *Chem. Rev.* **2012**, *112*, 2286.

[22] W. D. Dozier, J. S. Huang, L. J. Fetters, *Macromolecules* **1991**, *24*, 2810.

[23] a) A. E. Nel, L. Maedler, D. Velegol, T. Xia, E. M. V. Hoek, P. Somasundaran, F. Klaessig, V. Castranova, M. Thompson, *Nat. Mater.*

ADVANCED
SCIENCE NEWS

www.advancedsciencenews.com

ADVANCED
MATERIALS

www.advmat.de

2009, *8*, 543; b) A. Nino-Pariente, V. J. Nebot, M. J. Vicent, *Curr. Pharm. Des.* **2016**, *22*, 1274; c) C. J. Cheng, G. T. Tietjen, J. K. Saucier-Sawyer, W. M. Saltzman, *Nat. Rev. Drug Discovery* **2015**, *14*, 239.

[24] a) J. R. Moffat, I. A. Coates, F. J. Leng, D. K. Smith, *Langmuir* **2009**, *25*, 8786; b) M. Talelli, M. Barz, C. J. F. Rijcken, F. Kiessling, W. E. Hennink, T. Lammers, *Nano Today* **2015**, *10*, 93; c) J. W. Li, J. M. A. Carnall, M. C. A. Stuart, S. Otto, *Angew. Chem., Int. Ed.* **2011**, *50*, 8384; d) A. Pal, M. Malakoutikhah, G. Leonetti, M. Tezcan, M. Colomb-Delsuc, N. Van Duc, J. van der Gucht, S. Otto, *Angew. Chem., Int. Ed.* **2015**, *54*, 7852.

[25] L. Albertazzi, D. van der Zwaag, C. M. A. Leenders, R. Fitzner, R. W. van der Hofstad, E. W. Meijer, *Science* **2014**, *344*, 491.

[26] M. Barz, A. Duro-Castano, M. J. Vicent, *Polym. Chem.* **2013**, *4*, 2989.

[27] L. Albertazzi, F. J. Martinez-Veracoechea, C. M. A. Leenders, I. K. Voets, D. Frenkel, E. W. Meijer, *Proc. Natl. Acad. Sci. USA* **2013**, *110*, 12203.

[28] a) V. J. Nebot, B. Escuder, J. F. Miravet, J. Smets, S. Fernandez-Prieto, *Langmuir* **2013**, *29*, 9544; b) R. Novoa-Carballal, E. Fernandez-Megia, C. Jimenez, R. Riguera, *Nat. Prod. Rep.* **2011**, *28*, 78.

[29] a) R. Duncan, S. C. W. Richardson, *Mol. Pharmaceutics* **2012**, *9*, 2380; b) I. Canton, G. Battaglia, *Chem. Soc. Rev.* **2012**, *41*, 2718.

[30] R. Duncan, *Nat. Rev. Cancer* **2006**, *6*, 688.

[31] G. Sahay, D. Y. Alakhova, A. V. Kabanov, *J. Controlled Release* **2010**, *145*, 182.

[32] K. Palucka, J. Banchereau, *Nat. Rev. Cancer* **2012**, *12*, 265.

[33] a) H. Cabral, J. Makino, Y. Matsumoto, P. Mi, H. Wu, T. Nomoto, K. Toh, N. Yamada, Y. Higuchi, S. Konishi, M. R. Kano, H. Nishihara, Y. Miura, N. Nishiyama, K. Kataoka, *ACS Nano* **2015**, *9*, 4957; b) I. Mellman, G. Coukos, G. Dranoff, *Nature* **2011**, *480*, 480; c) S. De Koker, J. Cui, N. Vanparijs, L. Albertazzi, J. Grooten, F. Caruso, B. G. De Geest, *Angew. Chem., Int. Ed.* **2016**, *55*, 1334; d) S. De Koker, B. N. Lambrecht, M. A. Willart, Y. van Kooyk, J. Grooten, C. Vervaet, J. P. Remon, B. G. De Geest, *Chem. Soc. Rev.* **2011**, *40*, 320; e) S. T. Koshy, D. J. Mooney, *Curr. Opin. Biotechnol.* **2016**, *40*, 1.

[34] C. Li, S. Wallace, *Adv. Drug Delivery Rev.* **2008**, *60*, 886.

[35] N. L. Trevaskis, L. M. Kaminskas, C. J. H. Porter, *Nat. Rev. Drug Discovery* **2015**, *14*, 781.

[36] D. J. Irvine, M. C. Hanson, K. Rakhra, T. Tokatlian, *Chem. Rev.* **2015**, *115*, 11109.

[37] K. D. Wilson, S. G. Raney, L. Sekirov, G. Chikh, S. D. deJong, P. R. Cullis, Y. K. Tam, *Int. Immunopharmacol.* **2007**, *7*, 1064.

[38] D. N. Mastronarde, *J. Struct. Biol.* **2005**, *152*, 36.

[39] J. R. Kremer, D. N. Mastronarde, J. R. McIntosh, *J. Struct. Biol.* **1996**, *116*, 71.

[40] R. K. Heenan, *Rutherford Appleton Lab. Rep.*, RAL-89-129, **1989**.

[41] a) C. C. Tsou, S. S. Sun, *Org. Lett.* **2006**, *8*, 387; b) T. Tu, W. Fang, X. Bao, X. Li, K. H. Dötz, *Angew. Chem., Int. Ed.* **2011**, *50*, 6601.

[42] F. R. Martin, M. A. Caamaño, A. Aguilar, in *Biofarmacia y Farmacocinética. Ejercicios y Problemas Resueltos, 2nd Ed.*, Elsevier, Barcelona, Spain, **2014**.

1702888 (12 of 12)